



Impact of thermal and differential-preferential diffusion on the dynamics and acoustics of hydrogen–air slit flames

Borja Pedro-Beltran ^a,* Zin Shahin ^a, Matthias Meinke ^{a,c}, Sohel Herff ^b, Dominik Krug ^a, Wolfgang Schröder ^{a,c}

^a Institute of Aerodynamics and Chair of Fluid Mechanics, RWTH Aachen University, Wüllnerstraße 5a, 52062 Aachen, Germany

^b Jülich Supercomputing Centre, Forschungszentrum Jülich GmbH, Wilhelm-Johnen-Str., Jülich 52425, Germany

^c JARA Center for Simulation and Data Science, RWTH Aachen University, Seffenter Weg 23, 52074 Aachen, Germany

ARTICLE INFO

Keywords:

Combustion
Acoustics
Thermoacoustics
Hydrogen
CFD
DNS

ABSTRACT

The influence of thermal and differential-preferential diffusion on the flame dynamics and acoustic emission of laminar hydrogen–air slit flames is investigated using two-dimensional direct numerical simulations (DNS) and modal decomposition techniques. Simulations span a range of equivalence ratios ($\phi = 0.4\text{--}0.7$) and diffusion models, including mixture-averaged diffusion with and without the Soret effect and a simplified Unity Lewis number approximation. Proper Orthogonal Decomposition (POD) and Dynamic Mode Decomposition (DMD) reveal that dominant hydrodynamic instabilities persist across models, particularly at richer conditions. However, the inclusion of Soret and differential-preferential diffusion modifies the spectral structure of the dominant modes, such that energy is redistributed across higher-order components and a shift in the acoustic peak frequency is induced. These effects occur across all equivalence ratios, but are most evident at intermediate values where competing instabilities increase sensitivity to diffusion-driven modal interactions. At lean conditions, diffusion drives the dominant instability, while at richer conditions it modulates the spectral features of hydrodynamic modes. Neglecting thermal and differential-preferential diffusion fails to capture this behavior, potentially leading to underestimated sound levels at key hydrodynamic frequencies. These findings highlight the importance of detailed diffusion modeling to accurately predict combustion generated noise in hydrogen systems.

Novelty and significance statement

The present study is the first to provide a detailed numerical analysis of the effects of differential-preferential and thermal diffusion on the dynamics and acoustic emissions of hydrogen–air slit flames. The novelty of this work lies in two main contributions. First, it demonstrates that diffusion model assumptions can substantially alter predicted instability growth rates and spatial organization in slit flames. Second, it establishes a clear link between these modeling-induced changes in instability behavior and measurable differences in the resulting acoustic field, essential for accurate prediction of flame dynamics and acoustic response.

1. Introduction

The global transition to cleaner energy sources has renewed interest in hydrogen as a carbon-free alternative to fossil fuels. Hydrogen can be produced from renewable sources and combusted without generating CO₂, making it an attractive fuel for decarbonizing power generation and propulsion. However, the combustion characteristics of hydrogen differ significantly from those of conventional hydrocarbon fuels. The differences present unique challenges for stable and efficient energy conversion [1]. These arise since hydrogen has high diffusivity, broad

flammability limits, and a laminar burning velocity up to an order of magnitude greater than methane [2]. These properties strongly influence flame dynamics and can intensify the interaction between unsteady heat release and acoustic waves in combustors [3]. Such coupling may lead to thermoacoustic instabilities, where pressure waves and heat release interact to produce self-excited oscillations [4]. These instabilities result from the combined effects of fluid flow, chemical kinetics, and acoustics and are a concern in gas turbines using hydrogen-enriched or pure hydrogen fuels [5]. Pure hydrogen flames,

* Correspondence to: Wüllnerstraße 5a, Aachen, 52062, Germany.
E-mail address: b.pedro@aia.rwth-aachen.de (B. Pedro-Beltran).

with even higher burning velocities and diffusivity than blends, often couple strongly with acoustics and show a greater tendency toward high-frequency instabilities if not properly controlled [6]. However, hydrogen does not invariably worsen thermoacoustic instability. Its influence depends on configuration and operating conditions [7].

In addition to the system-level thermoacoustic feedback, hydrogen flames are also prone to hydrodynamic and diffusion-driven instabilities, which arise from the interplay of flow perturbations, density gradients, and species diffusion. The large thermal expansion across the flame creates a sharp density drop that makes the flame front susceptible to the hydrodynamic Darrieus–Landau (DL) instability [8]. DL instabilities amplify small wrinkles on the flame surface, increasing surface area and accelerating the flame. In shear layers, the strong velocity gradients typical of injectors and swirlers can further excite Kelvin–Helmholtz roll-up, enhancing flame wrinkling and promoting local extinction/reignition [9]. Hydrogen’s high laminar burning velocity and diffusivity make these effects more pronounced, since the flame can rapidly respond to flow perturbations and propagate into vortical structures [10].

Diffusion-driven instabilities arise from the unique diffusive properties of hydrogen and play an important role even when thermoacoustic feedback is controlled. In the classical literature (e.g., Williams, Combustion Theory [11]), these effects are collectively referred to as diffusional–thermal instabilities, originating from unequal heat and mass diffusion rates. In the present study, we distinguish between two aspects for clarity: differential diffusion, referring to disparities between mass and thermal diffusivities (i.e., non-unity Lewis number effects), and preferential diffusion, which describes species-specific diffusion differences ($D_i \neq D_j$). Where convenient, we refer to the combined action of differential (non-unity Lewis) and preferential diffusion as differential–preferential diffusion. For temperature–gradient–driven species transport, we use the term Soret effect (thermal diffusion of species). Collectively, we refer to differential–preferential diffusion and the Soret effect as non-equidiffusion. These mechanisms jointly contribute to the complex diffusion-driven instability behavior characteristic of hydrogen flames. For reference, the Lewis number is the ratio of thermal to mass diffusivity, $Le = \alpha/D$ (species-specific $Le_i = \alpha/D_i$). In lean hydrogen–air mixtures, the effective Lewis number is governed by the deficient species, i.e., hydrogen, which has $Le_{H_2} < 1$ [12]. Under such conditions, differences in diffusion rates alter local flame temperatures depending on flame stretch, leading to higher-than-adiabatic temperatures for positive stretch and lower-than-adiabatic temperatures for negative stretch [13].

To mitigate NO_x emissions, lean hydrogen–air mixtures are commonly employed because of their lower adiabatic flame temperatures [14]. However, such conditions amplify transport-driven effects, making thermodiffusive instabilities particularly important in practical combustors. The rapid diffusion of hydrogen relative to oxygen creates local equivalence ratio fluctuations, destabilizing the flame front and promoting intrinsic thermodiffusive instabilities [1]. These instabilities modify flame shape, enhance wrinkling, and lead to spatially and temporally varying heat release. The resulting unsteady heat release can generate pressure perturbations that couple with the natural acoustic modes of the combustor [15], potentially triggering thermoacoustic instabilities that pose risks such as structural vibration, noise, and component damage if not accurately predicted and controlled.

Predictions of flame-acoustic interactions in hydrogen flames are highly sensitive to transport properties, especially the Lewis number, and to the inclusion of thermal diffusion, i.e., the Soret effect. The slit flame or slot burner configuration has emerged as a canonical setup for experimentally and numerically analyzing such interactions in premixed flames. Some studies have focused on the role of Lewis number and transport modeling. For example, it was shown in [16] that increasing Le in acoustically excited laminar slit flames increases sound production, though the pressure response to flame surface fluctuations was found to be low or inconsistent. Separately, studies of

flame structure and hydrodynamics have highlighted the role of gas expansion and shear-layer interactions in early-stage wrinkling, with implications for reduced-order modeling [17,18]. Recent experiments report that Lewis-number effects are stronger in hydrogen than in methane, with pronounced coupling between flow fluctuations and local heat release near the flame tip [19]. In multi-slit laminar flames, differences in flame-tip behavior can dominate the flame transfer function (FTF) when $Le \geq 1$ [20]. Furthermore, distinct cellular structures and persistent pocket shedding across equivalence ratios have been linked to strong pressure fluctuations at the tip [21]. In addition, recent work suggests that including thermal diffusion and using physically more detailed transport models significantly affects predictions of flame behavior, especially in lean laminar regimes [1,22]. Yet, the influence of thermal diffusion and diffusion modeling assumptions on flame-acoustic coupling and thermoacoustic instability remains underexplored in the literature.

To address these gaps, a wide-slit H_2 /air flame is examined in the intrinsically unstable regime, allowing wrinkling, pocket shedding, and pressure oscillations to develop without external forcing. This canonical configuration limits confinement effects and makes the influence of transport processes, i.e., differential-preferential and thermal diffusion, clearly observable. The objective is to quantify how the diffusion model modifies the selection and growth of intrinsic instabilities and the convection of surface wrinkles, and how these modifications manifest in the emitted acoustic field.

This study is organized as follows. In Sections 2 and 3, the numerical methods and simulation setup are introduced. In Section 4, the effect of the diffusion model on the slit flames is discussed in detail. Finally, conclusions are given.

2. Numerical methods

2.1. General approach and modeling

The numerical framework comprises several key components: (1) the governing conservation equations, (2) spatial and temporal discretization schemes, (3) thermodynamic property evaluation, (4) transport coefficient calculation, and (5) chemical reaction modeling. The evolution of the field variables is determined by the fully compressible Navier–Stokes equations for reacting flows [23].

The equations are discretized using a conservative finite-volume approach. The variables are reconstructed at the surfaces using a MUSCL scheme for conservation laws [24]. Advection fluxes are also computed by a modified advection upstream splitting method (AUSM) [25], while the viscous fluxes are calculated via a central difference scheme. Time integration is performed by a five-stage, second-order accurate predictor–corrector Runge–Kutta scheme that is stability-optimized and well suited for efficient multi-physics coupling [26].

Heat capacities are evaluated as a function of temperature using the NASA7 coefficients [27]. The diffusive mass flux of species k is modeled by

$$\mathbf{j}_k = -\rho D_{k,m} \nabla Y_k - D_k^{\text{th}} \frac{\nabla T}{T}, \quad (1)$$

where $D_{k,m}$ is the effective species diffusion coefficient and D_k^{th} is the thermal diffusion coefficient accounting for the Soret effect. The species viscosity μ_k and thermal conductivity λ_k are also required to close the transport formulation. These transport properties are evaluated using three diffusion modeling approaches of decreasing physical fidelity, enabling a systematic isolation of the effects of differential-preferential and thermal diffusion.

1. “W. Soret” employs the mixture-averaged diffusion model [28], including thermal diffusion which captures the Soret effect.
2. “W/o. Soret” uses the same model but neglects thermal diffusion, i.e., $D_k^{\text{th}} = 0$ in Eq. (1).

3. “Unity Lewis” assumes equal thermal and mass diffusivity for all species (i.e., $Le_k = 1$) and neglects thermal diffusion.

Thermal diffusion coefficients D_k for hydrogen species (H and H₂) in the mixture-averaged Soret effect model are computed following the methodology described in [29]. The numerical framework has been previously validated for both laminar and turbulent cases [18,30]. The reactive solver and the implementation of the reduced Soret model are validated in the Supplementary Material and in [31].

The chemical source-term formulation follows the standard reactive-flow kinetics in [28]. The detailed H₂/air mechanism of Li et al. [32] is used, which specifies the reactions and thermochemical data used by the solver. It includes 9 species and 19 elementary and intermediate reactions. Vance et al. [33] showed that this mechanism yields only minor deviations in flame dynamics and tracked flame position in dynamically stabilized H₂/air flames in narrow channels when compared to the Konnov mechanism, which includes 15 species. Reaction rates and the corresponding analytic Jacobian are evaluated using code generated by pyJac [34].

In the discretization scheme used, the explicit time step is constrained by stability,

$$\Delta t \leq \min(\Delta t_{\text{adv}}, \Delta t_{\text{diff}}, \Delta t_{\text{acoustics}}, \Delta t_{\text{chem}}),$$

For lean H₂-air combustion, the chemical Jacobian yields very small Δt_{chem} , which makes the semi-discrete system stiff if chemistry is treated explicitly. Therefore, operator splitting is used: transport is advanced explicitly under the acoustic CFL condition, while chemistry is integrated implicitly using pyJac-generated rates and analytic Jacobians for the Li et al. mechanism [32,34], thereby removing the chemical time step restriction from the global stability limit. The transport equations are solved using the simulation framework m-AIA (multiphysics - Aerodynamisches Institut Aachen) [35], while the chemical kinetics are treated separately through a novel coupling of pyJac [34] and SUNDIALS [36].

2.2. Data analysis

2.2.1. Proper Orthogonal Decomposition

Proper Orthogonal Decomposition (POD) is a standard tool for extracting dominant coherent structures from high-dimensional data and for constructing low-dimensional representations that capture most of the flow variability [37]. Given a collection of snapshots of a spatially distributed field (here, the vectorized heat release rate (HRR)), POD seeks an orthonormal basis that maximizes captured variance.

The snapshot matrix V_1^N is formed by stacking the spatial data computed on consecutive snapshots in contiguous columns

$$V_1^N = [v_1, v_2, \dots, v_N] \in \mathbb{R}^{M \times N}, \quad v_i \in \mathbb{R}^M, \quad (2)$$

where M is the number of spatial degrees of freedom and N the number of snapshots. The POD is performed via the singular value decomposition (SVD) of the snapshot matrix. Specifically, the SVD is formed

$$V_1^N = U \Sigma Z^T, \quad (3)$$

where $U \in \mathbb{R}^{M \times r}$ and $Z \in \mathbb{R}^{N \times r}$ have orthonormal columns, $\Sigma = \text{diag}(\sigma_1, \dots, \sigma_r)$ with $\sigma_1 \geq \dots \geq \sigma_r > 0$, and $r = \text{rank}(V_1^N)$. The columns of U are the spatial POD modes, and the corresponding temporal coefficients are obtained by

$$A = \Sigma Z^T, \quad (4)$$

so that the i th row of A gives the time series of mode i . The modal energies are proportional to σ_i^2 , and the fraction of energy captured by the first k modes is $\sum_{i=1}^k \sigma_i^2 / \sum_{i=1}^r \sigma_i^2$.

Orthogonality is defined with respect to the discrete Euclidean inner product on the vectorized field, $\langle \mathbf{a}, \mathbf{b} \rangle = \mathbf{a}^T \mathbf{b}$. On nonuniform meshes, a strictly L^2 -consistent inner product can be enforced by introducing

spatial weights $W_e = \text{diag}(\Delta V_j)$ and applying the SVD to $W_e^{1/2} V_1^N$, with modes $W_e^{-1/2} U$. Note that we do not use this weighting. Since the POD region is discretized on a uniform grid, the Euclidean inner product is equivalent to a discrete L^2 inner product up to the constant cell volume, which does not affect orthogonality or relative modal energies. Thus, the leading POD modes identified provide compact, physically interpretable structures, e.g. shear layers, breathing/convecting patterns, or instability signatures ordered by their contribution to the dataset variance.

2.2.2. Dynamic mode decomposition

While POD extracts spatial modes ranked by their energy content, it does not directly associate them with specific temporal dynamics. Dynamic Mode Decomposition (DMD) complements POD by identifying spatial structures tied to single frequencies and growth rates, thus providing a spectrally resolved view of the coherent motions. Similarly to POD, a snapshot matrix V_1^N is formed with the spatial data.

Following the method introduced by Schmid [38], DMD is applied to the sequence of instantaneous heat release rate (HRR) fields, arranged into two snapshot matrices $V_1^{N-1} = [v_1, v_2, \dots, v_{N-1}]$ and $V_2^N = [v_2, v_3, \dots, v_N]$. These matrices are related through a linear mapping $V_2^N \approx A V_1^{N-1}$, where $A \in \mathbb{C}^{m \times m}$ is the full DMD operator advancing one snapshot to the next. To avoid forming A explicitly, a reduced operator is obtained by projecting A onto the subspace spanned by the left singular vectors U of the SVD of $V_1^{N-1} = U \Sigma W^*$. In the present analysis, the singular value decomposition of V_1^{N-1} is carried out in full rank, i.e. without truncation of the singular spectrum. The reduced operator $F_{\text{DMD}} \in \mathbb{C}^{(N-1) \times (N-1)}$ is therefore obtained by projection onto the POD subspace defined by U

$$F_{\text{DMD}} = U^* A U = U^* V_2^N W \Sigma^{-1}, \quad (5)$$

which is consistent with the standard “exact DMD” formulation.

Its eigendecomposition provides the DMD modes and eigenvalues:

$$F_{\text{DMD}} Y = Y \Lambda, \quad (6)$$

where $\Lambda = \text{diag}(\mu_n)$ are the Ritz eigenvalues and columns of Y are the eigenvectors. To reconstruct the flow field, DMD modes are obtained by

$$\Phi = V_1^{N-1} W \Sigma^{-1} Y, \quad (7)$$

which is equivalent to $\Phi = U Y$, as $V_1^{N-1} W \Sigma^{-1} = U$. The snapshots are represented as

$$v_i = \sum_{n=1}^{N-1} a_n \mu_n^{i-1} \phi_n, \quad i = 1, \dots, N-1, \quad (8)$$

where a_n are the optimal amplitudes. Furthermore, each eigenvalue μ_n can be expressed in polar and exponential form

$$\begin{aligned} \mu_n &= r_n e^{i\theta_n} = e^{\lambda_n \Delta t}, \\ \lambda_n &= \frac{\ln(\mu_n)}{\Delta t} = \frac{\Re(\ln(\mu_n))}{\Delta t} + i \frac{\Im(\ln(\mu_n))}{\Delta t}, \end{aligned} \quad (9)$$

The quantity λ_n represents the continuous-time eigenvalue corresponding to the discrete-time eigenvalue μ_n , characterizing growth/decay and oscillatory behavior. A negative real part of λ_n indicates a decaying mode, a positive part suggests growth, and a zero real part corresponds to neutral stability. The imaginary part λ_i of the complex frequency contains information about the temporal periodicity of the DMD mode. The frequency in the DMD mode can be computed by

$$f = \Im(\ln \mu_n) / 2\pi \Delta t. \quad (10)$$

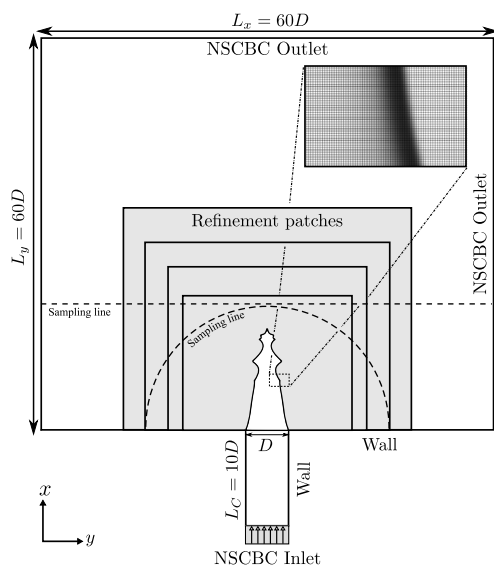


Fig. 1. Computational domain of the slit flame. Inlet (bottom) and outlets (top, left, right) are given as NSCBCs. The grid is refined in the vicinity of the flame, with gradually decreasing mesh refinement levels. Sampling lines and refinement patches are shown schematically and are not to scale.

3. Simulation setup

To explore the inherent instabilities of premixed hydrogen–air flames and their associated acoustic emissions, a series of two-dimensional direct numerical simulations (2D DNS) of laminar slit flames are performed. Since a fully compressible solver is employed to resolve acoustic pressure propagation, the time step is on the order of 3×10^{-8} s, making the computational cost substantial and therefore, the present study is limited to two dimensions. The simulations span a range of fuel–air equivalence ratios $\phi = \{0.4, 0.5, 0.6, 0.7\}$, and incorporate three diffusion models: mixture-averaged with Soret diffusion (W. Soret) [28,29], mixture-averaged without Soret effects (W/o. Soret), and a simplified Unity Lewis number formulation (Unity Lewis). The chosen equivalence ratio range is representative of practical lean premixed hydrogen combustion. Even the richer cases considered ($\phi = 0.6$, $\phi = 0.7$) achieve significant NO_x reductions, reaching values several orders of magnitude lower than in stoichiometric flames [14].

All simulations are conducted at a constant ratio of inlet velocity to laminar flame speed, $u_\infty/s_L = 6$, across all cases. This ensures that the flame length remains comparable across all equivalence ratios and modeling approaches. More fundamentally, fixing u_∞/s_L maintains consistent dimensionless flow and stretch conditions. For a steady slit flame, the kinematic balance $s_L = u_\infty \sin \alpha$ directly relates the cone angle α to u_∞/s_L , while the local stretch rate scales as $K \sim s_L/D$, where D is the channel width, yielding a dimensionless stretch $\chi = K\delta_L/s_L \sim \mathcal{O}(\delta_L/D)$ that remains effectively constant for the different cases. Consequently, the flame-stretch response $s_n/s_L \approx 1 - \text{Ma} \chi$, where Ma is the Markstein number, varies with equivalence ratio only through changes in Ma and mixture transport properties, not due to geometric effects. Thus, this scaling approach isolates the impact of differential-preferential and thermal diffusion on flame dynamics while maintaining a comparable stretch environment [39,40].

Ambient conditions are $T = 291$ K and $p = 1$ bar. Analyses are performed after the flow reaches a statistically steady limit cycle. Each case is initialized by mapping a 1-D laminar flame solution with profiles of T , ρ , Y_k , and u onto the 2-D domain as a planar segment near the channel exit. The front is then convected and develops under fully 2-D dynamics. The transient to the permanent regime typically requires 3×10^5 – 5×10^5 time steps. Then, we collect data over an additional $\mathcal{O}(10^6)$

time steps for statistics. The number of cycles depends on ϕ because u_∞/s_L is held fixed across cases. Consequently, the oscillation period varies with ϕ . Approximately 10 cycles are analyzed for the leanest case ($\phi = 0.4$) and about 20 for the richest ($\phi = 0.7$).

The computational domain shown in Fig. 1 includes the entire inlet plenum and upstream channel to ensure that inlet perturbations and their effects are fully resolved [41]. The domain dimensions are $L_x = L_y = 60D$, where $D = 1$ cm denotes the channel width. The slit width used here ($D = 1$ cm) is an order of magnitude larger than in prior studies ($D \sim 1$ mm; [42,43]). The wider geometry reduces wall damping and increases residence time, which makes it easier to identify the effects of non-equidiffusion and their interaction with Darrieus–Landau instabilities, leading to self-sustained oscillations.

To prevent artificial pressure-wave reflections, Navier–Stokes characteristic boundary conditions (NSCBC) are applied at all inlet and outlet boundaries following [44]. Incoming waves are not set to zero. Instead, they are computed using relaxation coefficients to prevent drift while maintaining low reflection. The relaxation coefficients used for the inlet and outlet are $\eta_5 = 1.5$ and $\eta_1 = 0.3$. These non-reflecting conditions minimize the formation of spurious standing waves that could otherwise interfere with flame dynamics and distort the development of intrinsic instabilities.

Local grid refinement is used near the flame to resolve steep gradients in the reaction zone, while a coarser mesh is employed in the far field. The flame front is resolved by at least 15 cells across the flame for all cases. Sampling lines are placed both along the flame front and in the acoustic field to monitor heat release rate fluctuations and pressure signals.

4. Results

To evaluate the impact of transport modeling on flame dynamics, cellular structure, and acoustic response, a comparative analysis of the selected fuel–air equivalence ratios and diffusion model formulations is presented. First, the overall flame topology and key quantitative properties are examined to establish a baseline understanding of how each model alters global flame characteristics across equivalence ratios. An analysis of the cellular flame structure follows, focusing on flame front features and the distribution of local curvature scales. Next, the acoustic field is assessed through spectral analysis of pressure signals, followed by a detailed examination of the flame dynamics using POD, which reveals how diffusion models affect the energy distribution and spatial structure of coherent flame modes. Finally, DMD is applied to resolve the dominant frequencies and growth behavior of the unsteady flame structures, providing a complementary frequency-centric view of the flame dynamics and its acoustic coupling.

4.1. Flame topology and transport model effects

Fig. 2 shows instantaneous snapshots of the four flames at a fully developed stage for three diffusivity models: mixture-averaged with Soret diffusion (“W. Soret”), mixture-averaged without Soret (“W/o. Soret”), and Unity Lewis, which eliminates differential-preferential diffusion altogether. The ratio u_∞/s_L is held constant to isolate transport effects from residence-time variations.

As the mixture becomes richer, the relative influence of thermodynamic and hydrodynamic mechanisms shifts progressively. At $\phi = 0.4$, non-equidiffusive effects dominate. The Soret effect drives hydrogen toward hot, positively curved regions (Soret flux $\mathbf{J}_{\text{H}_2}^{\text{Sor}} \propto -D_{T,\text{H}_2} \nabla T$), thereby reinforcing the preferential diffusion mechanism. Fuel accumulates at cusps, locally increasing the consumption speed s_n and amplifying short-wavelength perturbations. Meanwhile, differential-preferential diffusion depletes fuel at the flame tips, producing open tips with very low or vanishing burning rates. Together, these effects create deep HRR minima behind cusps and super-adiabatic temperature pockets downstream due to strong local curvature. Removing

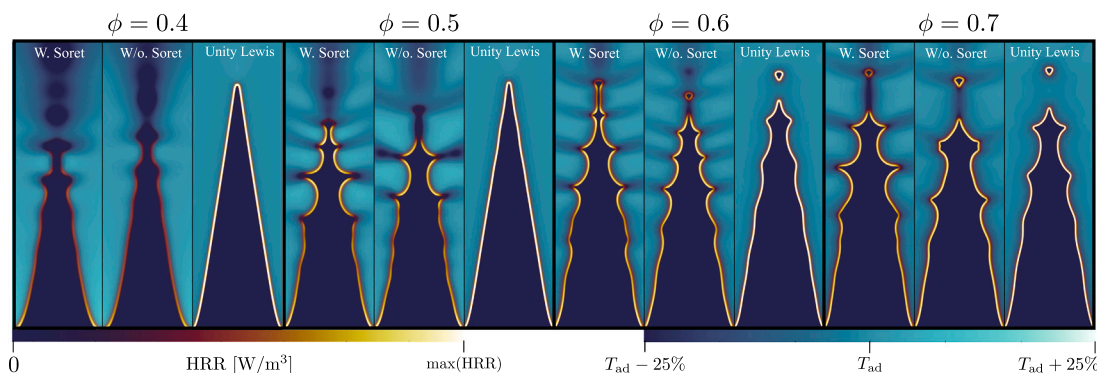


Fig. 2. Instantaneous heat release rate (HRR) and temperature contours for four equivalence ratios (blocks from left to right: $\phi = 0.4$ to 0.7). Each block includes different transport model: with Soret diffusion (W. Soret), without Soret diffusion (W/o. Soret), and Unity Lewis number (Unity Lewis). Temperature fields are shown with offsets relative to the respective adiabatic flame temperature. The quantity $\max(\text{HRR})$ denotes the maximum heat release rate in each case and is used for consistent visual scaling. HRR colorbar is shown with a transparency mapping option, so only the flame front region is visible. Animations of the HRR field for each flame are provided in the Supplementary Material. (For interpretation of the references to color in this figure legend, the reader is referred to the web version of this article.)

Soret diffusion (W/o. Soret) reduces this fuel-redistribution mechanism, yielding larger characteristic cell sizes, fewer secondary cusps, and shallower HRR valleys. The Unity Lewis case suppresses all differential-preferential diffusion effects, and the flame remains nearly planar throughout the simulation, with no cellular instabilities developing.

At $\phi = 0.5$, thermodiffusive instability remains active but weaker. The W. Soret case continues to redistribute hydrogen toward curved regions, though the main manifestation shifts from deep cusp penetration to increased cell density at a somewhat larger mean wavelength. The W/o. Soret case shows further coarsening of the cellular pattern with shallower HRR modulation, while the Unity Lewis case exhibits only small-amplitude, long-wavelength undulations near the tip region.

At $\phi = 0.6$, hydrodynamic instability becomes increasingly important, yet non-equidiffusive effects still strongly influence the flame structure. All three models exhibit wrinkles at scales comparable to the hydrodynamic length scale, which depends on the flame thickness and density ratio, but the resulting structures differ markedly. The W. Soret case shows sharper curvature peaks, more pronounced secondary structures along the flame front, and stronger spatial variations in heat release rate. These features indicate that thermal diffusion continues to amplify curvature-dependent effects and generate localized hot spots, even while hydrodynamic wrinkling governs the overall flame geometry. The W/o. Soret case displays intermediate behavior. It retains curvature-dependent modulation from differential-preferential diffusion but lacks the additional fuel redistribution caused by the Soret effect. The Unity Lewis case produces the smoothest flame surface and the most uniform heat release distribution, reflecting pure Darrieus–Landau dynamics without diffusion-driven amplification of local perturbations.

At $\phi = 0.7$, differential-preferential diffusion effects are much weaker as the mixture Lewis number increases, and hydrodynamic instability dominates the overall flame shape for all models. Nevertheless, the Soret effect remains active: the W. Soret case still exhibits curvature-dependent HRR variations and slightly sharper temperature gradients than the W/o. Soret case, while the W/o. Soret and Unity Lewis flames become increasingly similar. All models produce comparable large-scale structures, typically two broad lobes, with the primary dynamics governed by hydrodynamic instability.

In summary, at increasing equivalence ratio from 0.4 to 0.7, control shifts from short-wavelength thermodiffusive instability, which is strongly enhanced by Soret at lean conditions, to long-wavelength hydrodynamic instability. This transition explains the growth in the observed wrinkle scale and the partial convergence of the three transport models in their large-scale geometry, while thermodiffusive effects, particularly Soret-driven enrichment near positively curved regions,

continue to influence local burning rates even at $\phi \approx 0.6$ – 0.7 . This behavior is consistent with prior DNS of lean planar H_2/air flames [45], where Soret diffusion accelerates the onset of cellular structures and increases local heat-release rates in positively curved regions. Moreover, the overall burning efficiency is $\sim 10\%$ – 15% higher with Soret once secondary cells have formed, indicating that similar redistribution mechanisms likely act in the present slit-flame configuration.

The data in Table 1a, summarize the effects of the equivalence ratio (ϕ) and of the diffusion model on the key time-averaged flame characteristics for premixed H_2 -air flames. The mean flame length is defined as the distance from the flame base to the highest point along the $C = 0.5$ contour of the progress variable

$$C = \frac{T - T_\infty}{T_{\text{ad}} - T_\infty},$$

calculated from the temporally averaged flame profiles. The minimum and maximum flame length are evaluated from the $C = 0.2$ and $C = 0.8$ lines of the mean profile, respectively. Pockets shed from the tip leave the mean length unchanged, yet they increase the maximum length since their trace in the mean field is included when building the $C = 0.8$ contour. The flame angle is measured between the point of maximum gradient along the flame front and the vertical symmetry axis. As ϕ increases from 0.4 to 0.7, there is a clear trend of increasing flame length and flame angle, regardless of the transport model used.

When comparing the three modeling approaches, several consistent trends appear. The Unity Lewis model produces the longest flames and the widest mean flame angles, especially under lean conditions, indicating a suppression of differential-preferential diffusion effects. In the present setup, the inlet velocity scales with the laminar burning velocity, $u_\infty = C s_L(\phi, \text{model})$, so the bulk advection time $\tau_{\text{bulk}} = L_{\text{flame}}/u_{\text{bulk}} \approx L_{\text{flame}}/(C s_L)$ depends on both the flame length and the model dependent s_L . At $\phi = 0.4$, the Unity Lewis model yields a larger s_L than the mixture-averaged cases; despite the longer flame, the higher s_L leads to a smaller τ_{bulk} . At $\phi = 0.7$, the Unity Lewis model predicts a slightly lower s_L than the mixture-averaged model, so τ_{bulk} does not decrease and may even become comparable or larger. However, τ_{bulk} reflects only mean-flow advection and may not represent the actual propagation of wrinkles and perturbations along the flame surface, which can deviate significantly from the mean advection velocity. This distinction motivates the introduction of a wrinkle-based time scale.

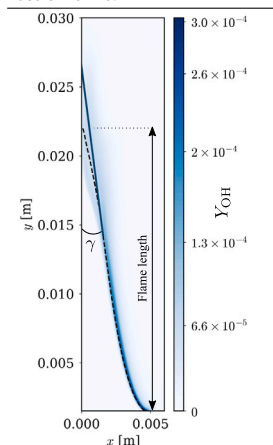
To quantify wrinkle advection along the flame surface, the mean flame position is extracted as an isocontour of $Y_{\text{H}_2\text{O}}$ at its half-maximum value. The instantaneous heat release rate perturbations $\text{HRR}'(s, t) = \text{HRR}_{\text{inst}}(s, t) - \text{HRR}(s)$ is projected onto this curve as a function of arc length s and time t . To isolate the left branch of the V-shaped flame and

Table 1

(a) Summary of key flame properties for premixed H₂-air simulations at various equivalence ratios (ϕ) using several diffusion models. Values include flame length (minimum/mean/maximum), flame angle γ , wrinkle advection time τ_{wrinkle} (in comparison to bulk flow convection time), and normalized maximum temperature $T_{\text{max}}/T_{\text{ad}}$. (b) An illustration of the time-averaged flame front represented by the OH mass fraction (Y_{OH}), which is used for the flame angle and flame length calculations. For cases in which no wrinkling is observed, the asterisk (*) denotes the normal advection time.

ϕ	Model	Flame length [mm] (min/mean/max)	Flame angle γ	τ_{wrinkle} [ms]	$T_{\text{max}}/T_{\text{ad}}$
0.4	W. Soret	18.9/22.1/25.8	7.29°	11.05 (-25%)	1.155
	W/o. Soret	21.3/24.1/26.9	6.75°	13.54 (-12%)	1.149
	Unity Lewis	27.9/29.6/30.2	8.41°	9.97* (/)	1.00
0.5	W. Soret	22.9/24.5/26.4	7.31°	6.62 (-2.5%)	1.136
	W/o. Soret	22.5/24.7/26.3	7.97°	7.15 (+4.5%)	1.101
	Unity Lewis	28.4/29.3/29.6	8.44°	6.0* (/)	1.00
0.6	W. Soret	25.5/27.4/29.1	7.33°	4.53 (-1.2%)	1.1208
	W/o. Soret	24.7/26.1/27.9	8.33°	4.58 (+4.5%)	1.084
	Unity Lewis	26.9/28.1/29.6	8.90°	4.48 (+3%)	1.00
0.7	W. Soret	26.5/28.1/30.0	7.54°	3.5 (+4.5%)	1.106
	W/o. Soret	25.3/26.8/28.7	8.43°	3.24 (+1%)	1.073
	Unity Lewis	26.3/27.3/29.1	8.85°	3.65 (+4.2%)	1.00

(a) Flame properties data



(b) Flame angle visualization

avoid interference from counter-propagating waves on the right branch, spatial points are filtered to $0 < x < D/2$. A Fast Fourier Transform is applied at each spatial location to identify the dominant oscillation frequency f_{dom} . The phase $\phi(s)$ at this frequency is extracted along the flame surface and unwrapped to avoid discontinuities. Regions near the burner lip where wrinkles have not yet formed and the phase remains nearly constant are excluded to ensure that only established wave propagation is analyzed. This occurs primarily at lean conditions where the wrinkle development length is significant relative to the flame height. The wrinkle advection speed is then computed from the phase gradient as $v_{\text{wrinkle}} = \omega/(d\phi/ds)$, where $\omega = 2\pi f_{\text{dom}}$ is the angular frequency. The computed wrinkle advection times τ_{wrinkle} are summarized in Table 1a. At lean conditions ($\phi = 0.4$), wrinkle propagation deviates significantly from bulk flow advection, with deviations up to 25% for the W. Soret case. These deviations diminish progressively with increasing equivalence ratio. At $\phi = 0.7$, all transport models show wrinkle advection times within a few percent of the bulk flow estimate.

The maximum temperature normalized by the adiabatic flame temperature $T_{\text{max}}/T_{\text{ad}}$ further illustrates the role of transport modeling. Values exceeding unity for the detailed transport cases reflect localized super-adiabatic conditions caused by non-equidiffusive effects, especially at lean conditions. The Unity Lewis model, by construction, limits $T_{\text{max}}/T_{\text{ad}}$ to 1. This emphasizes its inability to capture this important feature of hydrogen combustion. Overall, the results underscore that while Unity Lewis models can qualitatively reproduce general trends, they significantly underpredict the flame temperature due to neglecting the impact of differential-preferential diffusion, especially at leaner conditions. The inclusion of differential-preferential and thermodiffusion yields a more accurate and physically representative description of flame dynamics, which is particularly relevant to capture the details of the flame structure and of the intrinsic instability mechanisms.

4.2. Cellular structure distribution

Fig. 3(a) shows the normalized heat release rate (HRR), where HRR_{max} denotes the maximum HRR in the respective domain, together with the mass fraction of hydrogen radicals (Y_{H}), plotted along the flame front as a function of arc length normalized by the laminar flame thickness. HRR is evaluated on the isoline of the progress variable $C = 0.5$, which is indicated by the solid white line in the right panel. Several cusps can be identified along this line marked by red circles at locations where HRR drops sharply. Due to the high diffusivity of hydrogen, leaner mixtures tend to accumulate in cusp regions, while

richer mixtures appear in convex areas oriented toward the unburnt gases. This results in localized quenching and vanishing HRR inside the cusps which is observed clearly in Fig. 2. Following [46], the smallest cell size λ_{cell} is defined as the distance between two adjacent cusp tips. Assuming a semicircular shape for the flame front between cusps, λ_{cell} can be expressed as $\lambda_{\text{cell}} = 2l^*/\pi$, where l^* is the arc length between two curvature peaks along the flame front. It is illustrated in Fig. 3(a). The distribution of λ_{cell} for different equivalence ratios and transport models is presented in Fig. 3(b).

Clear shifts in the dominant length scale are observed as ϕ increases. For the $\phi = 0.4$ case, the case including thermodiffusion exhibits a bimodal distribution with peaks at normalized scales of approximately 2.5 and 4, while disabling the Soret effect yields a single peak near 3. The Unity Lewis model shows no cellular structures (see Fig. 2). The observed length scales at lean conditions are qualitatively consistent with the thermodiffusive cell sizes reported by Berger et al. [46] for freely propagating lean hydrogen flames, confirming that thermodiffusive instability is the dominant mechanism. However, the bimodal character in the W. Soret case and the somewhat larger normalized scales suggest additional modulation by the slit-flame configuration. Limited residence time restricts the development of the finest-scale cells, while velocity gradients and flame anchoring near the burner lip may promote coarser structures that coexist with thermodiffusive cells.

At $\phi = 0.5$, smaller structures dominate near 4, with cellular patterns persisting in both cases that retain differential-preferential diffusion effects, i.e., W. Soret and W/o. Soret. The absence of significant cellular structures in the Unity Lewis case confirms that hydrodynamic instabilities alone are insufficient to drive cell formation at this equivalence ratio. The contrast between these models reveals a transitional regime where differential-preferential diffusion ($Le \neq 1$) remains the primary driver of cellular structure, though its influence is weakening compared to the leaner condition. The Soret effect introduces additional modulation but does not fundamentally alter the dominant length scale. As ϕ increases to 0.6 and 0.7, the distribution shifts toward larger length scales and the spectrum broadens, particularly when non-equidiffusion is excluded. However, at $\phi = 0.7$, an additional effect emerges. Although non-unity-Lewis effects weaken as Le_{eff} increases and Markstein-number sensitivity diminishes, thermal diffusion still modulates the cell-size distribution. The Soret mechanism drives preferential transport of hydrogen toward high-temperature regions ($J_{\text{H}_2}^{\text{Sor}} \propto -D_{T,\text{H}_2} \nabla T$), maintaining curvature-dependent fuel redistribution even when stretch sensitivity from non-unity-Lewis effects has diminished.

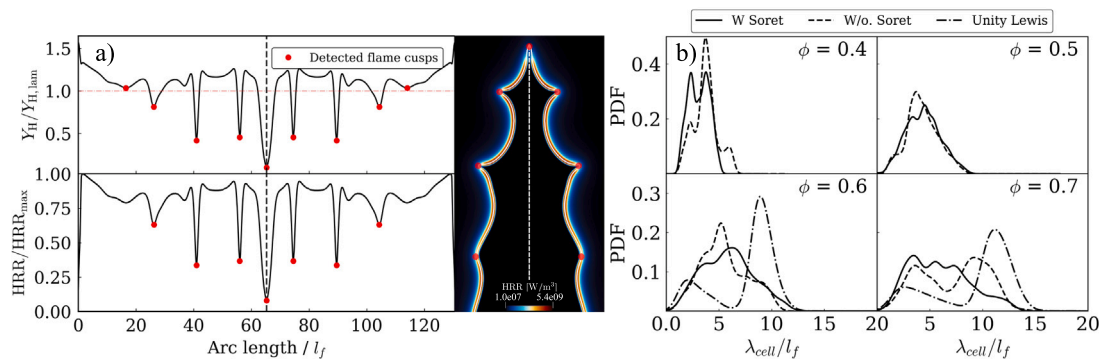


Fig. 3. (a) The normalized HRR (HRR_{max}) denotes the maximum heat release rate value in each case.) and element mass fraction of hydrogen (Y_H) with respect to the arc length of the flame isocontour at progress variable $C = 0.5$. Y_H normalized by the values of a laminar, unstretched premixed flame at T of isocontour. The laminar flame thickness normalizes the flame front curvature. Local minima in HRR, which correspond to flame cusps, are identified by red circles in the plot and shown on the corresponding flame contour image (right-hand side). b) Probability density functions (PDFs) of the normalized flame cell size, $\lambda_{\text{cell}}/l_f$, where l_f is the laminar flame thickness, for several equivalence ratios ($\phi = 0.4\text{--}0.7$) and diffusion models. PDFs are constructed from 300 snapshots spanning a total simulation time of 1.8×10^{-2} s, ensuring sufficient statistical resolution. Detailed statistics for PDF construction are provided in Table 1 in the Supplementary Material. (For interpretation of the references to color in this figure legend, the reader is referred to the web version of this article.)

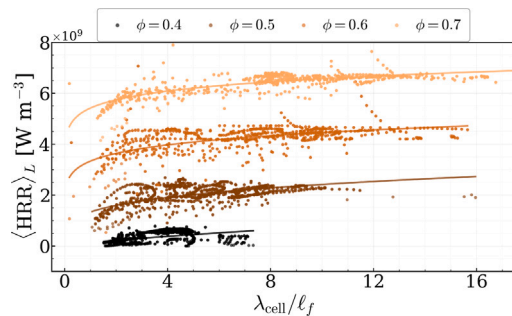


Fig. 4. Spatially averaged heat release rate ($\langle \text{HRR} \rangle_L$) versus normalized cellular flame structure size ($\lambda_{\text{cell}}/l_f$) for equivalence ratios $\phi = 0.4\text{--}0.7$ with Soret effect. The heat release rate is averaged over individual cellular structures. Power-law relationships fitted to the data are shown by the solid lines. (For interpretation of the references to color in this figure legend, the reader is referred to the web version of this article.)

Fig. 4 shows the distribution of the spatially averaged heat release rate $\langle \text{HRR} \rangle_L$ computed by spatially averaging the HRR over the arc segment between two consecutive cusps. This length-independent metric is evaluated over more than 150 snapshots for each flame case. A clear positive correlation is seen between the normalized cellular structure size $\lambda_{\text{cell}}/l_f$ and $\langle \text{HRR} \rangle_L$ across all equivalence ratios up to a certain length scale. Beyond this point, $\langle \text{HRR} \rangle_L$ remains nearly constant, even for larger cellular structures. Smaller cells consistently exhibit lower average heat release rates. For $\phi = 0.6$ and $\phi = 0.7$, a sharp drop in heat release is observed at very small scales when small cells form between larger cells. The surrounding structures deplete local fuel, which leads to insufficient reactant concentration for sustained combustion and gradual extinction of the smaller cell.

4.3. Sound pressure level

The observed acoustic spectra (Fig. 5) exhibit distinct frequency ranges that require interpretation in the context of established flame dynamics and sound generation mechanisms. The literature on laminar premixed flames identifies multiple physical processes that contribute to acoustic emission, each operating at characteristic time scales.

The broadband low-frequency emission observed across all cases is consistent with global flame dynamics. The characteristic convective time scale, $\tau \sim L_{\text{flame}}/u_{\text{bulk}}$, commonly used to describe the temporal response of laminar premixed flames [47], is adopted here as a

representative measure of the dominant flow time scale. Based on the wrinkle advection times in Table 1, τ_{wrinkle} ranges from 3.5 ms ($\phi = 0.7$) to 11.05 ms ($\phi = 0.4$), corresponding to frequencies of approximately 90–285 Hz, which is in agreement with the observed low-frequency content in Fig. 5. The similarity between these convective frequencies and the spectral peak range suggests that the low-frequency component arises from large-scale, quasi-periodic modulation of the entire flame structure, i.e. flame breathing. Such behavior reflects the global response of the flame–flow system, where variations in bulk flow rate and heat release feedback drive slow, spatially coherent oscillations of the mean reaction zone. These large-scale motions contrast with the higher-frequency fluctuations associated with fine-scale wrinkle formation and local curvature dynamics, which dominate the upper portion of the spectrum.

While the low-frequency content is associated with global breathing and large-scale oscillations of the entire flame, the more pronounced spectral peaks at intermediate frequencies, particularly at $\phi = 0.6$ and $\phi = 0.7$, point to additional, more localized unsteady processes. These features warrant comparison with documented flame tip dynamics. Studies of acoustically excited laminar flames have identified pocket formation and flame element separation as sources of acoustic emission [48]. Haghiri et al. [49] further showed that flame annihilation events, i.e., the mutual consumption of opposing flame elements, serve as efficient monopolar acoustic sources in turbulent premixed flames. Although the present flames are laminar and forced, similar tip dynamics involving periodic pocket shedding are observed (see Supplementary Material), suggesting an analogous mechanism for the observed acoustic peaks.

The variation in peak frequency across diffusion models provides insight into the underlying time scales: at $\phi = 0.6$, the dominant peak shifts by a 14% reduction from approximately 1200 Hz (Unity Lewis) to 1050 Hz (W. Soret). However, the wrinkle advection times vary by less than 5% between these cases (Table 1), indicating that bulk advection cannot explain the observed frequency shift. Instead, the acoustic frequency is set by local cellular dynamics involving multiple time scales. These include the time required for pockets to form and pinch off through flame consumption at the neck region and the oscillatory motion of the flame tip as it advances and retreats during pocket shedding. Physically, diffusion models influence the dynamics by modifying how rapidly local mixture gradients and curvature-induced variations in burning rate evolve. Therefore, differences in differential-preferential and thermal diffusion alter the characteristic time scale of pocket formation and tip oscillation, leading to the observed spectral shifts in acoustic emission, even though the global convective time scale remains nearly unchanged. These dynamics are directly influenced

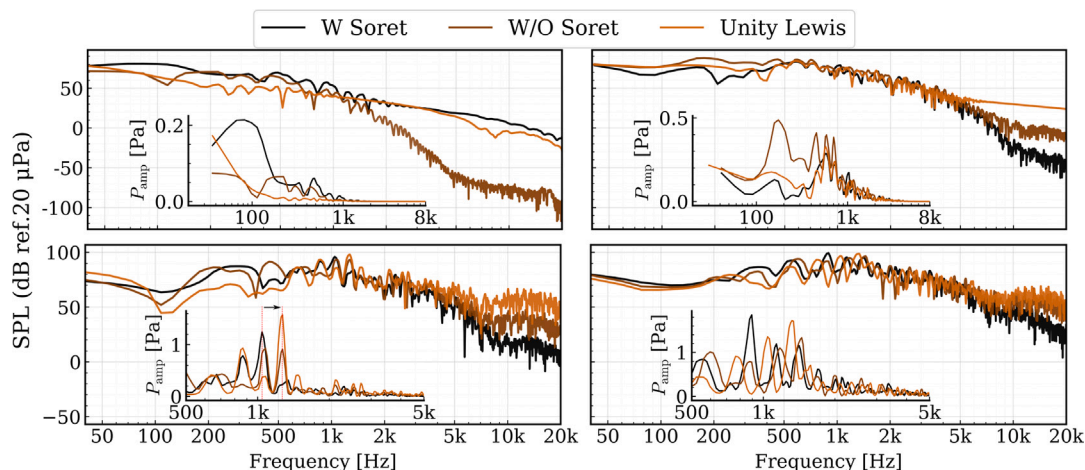


Fig. 5. Sound pressure level (SPL) spectra of the acoustic field for several equivalence ratios ($\phi = 0.4 - 0.7$) and diffusion models. Insets show the corresponding pressure amplitude spectra (P_{amp}). Note the different scaling in the insets. (For interpretation of the references to color in this figure legend, the reader is referred to the web version of this article.)

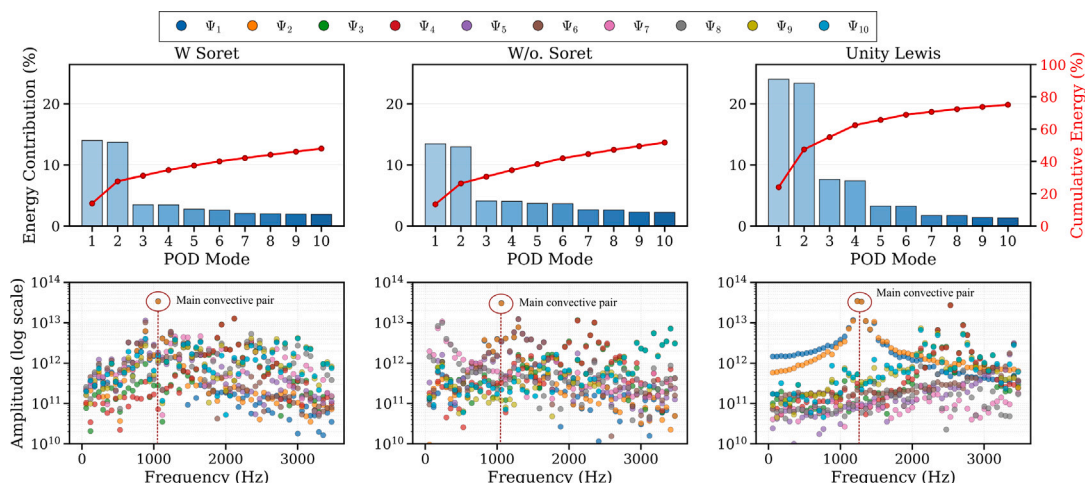


Fig. 6. POD analysis of the heat release rate perturbation field for a fixed equivalence ratio $\phi = 0.6$ for several diffusion models. The top row shows the energy contribution of the first ten POD modes, with cumulative energy plotted in red. The bottom row presents the frequency spectra of the temporal coefficients for each mode. (For interpretation of the references to color in this figure legend, the reader is referred to the web version of this article.)

by curvature-dependent consumption rates arising from differential-preferential and thermal diffusion, which modify the temporal response of the flame beyond what global convective transport alone would predict.

Furthermore, thermodiffusive instabilities in hydrogen flames are known to exhibit intrinsic temporal behavior. Berger et al. [46] showed that such instabilities possess dispersion relations $\sigma(\kappa)$ linking growth rate and oscillation frequency to perturbation wavenumber with the imaginary component determining characteristic oscillation frequencies of unstable modes. While their analysis considers planar and freely propagating flames, it demonstrates that cellular structures have inherent time scales not prescribed by the flow, which naturally influence the frequencies at which flame-acoustic coupling occurs in the present configuration. The cellular flame structure influences acoustic characteristics through its impact on heat release fluctuations since premixed flames can be represented acoustically as distributions of monopole sources [50] with sound pressure determined by the second time derivative of total reacting volume. While small variations appear at higher frequencies, they remain less significant in comparison to the dominant features associated with pocket shedding and flame-tip oscillations.

4.4. POD analysis

The proper orthogonal decomposition (POD) of the heat release rate field reveals the dominant spatial structures and their temporal evolution that cause unsteady flame dynamics. Each POD mode represents a spatially coherent structure, while the corresponding temporal coefficient encodes its time-dependent amplitude. The energy content of each mode reflects its statistical importance in reconstructing the dataset, and the spectrum of its temporal coefficient provides insight into the frequency range of the associated dynamics. This framework allows the decomposition of the complex flame behavior into interpretable physical contributions, ordered by their relative significance.

Theoretically, a traveling wave cannot be captured by a single real-valued POD mode [51]. Since POD operates on real-valued fields, any traveling or convecting structure, i.e., one with spatial and temporal phase, requires a pair of orthogonal modes with nearly equal energy, similar shape, and phase-shifted temporal coefficients. These paired modes allow the construction of sine-cosine combinations that capture the phase rotation which is required to describe wave propagation. In contrast, breathing or pulsating modes are typically characterized by a symmetric shape and appear as isolated POD modes, lacking a partner due to the absence of directional phase progression. These

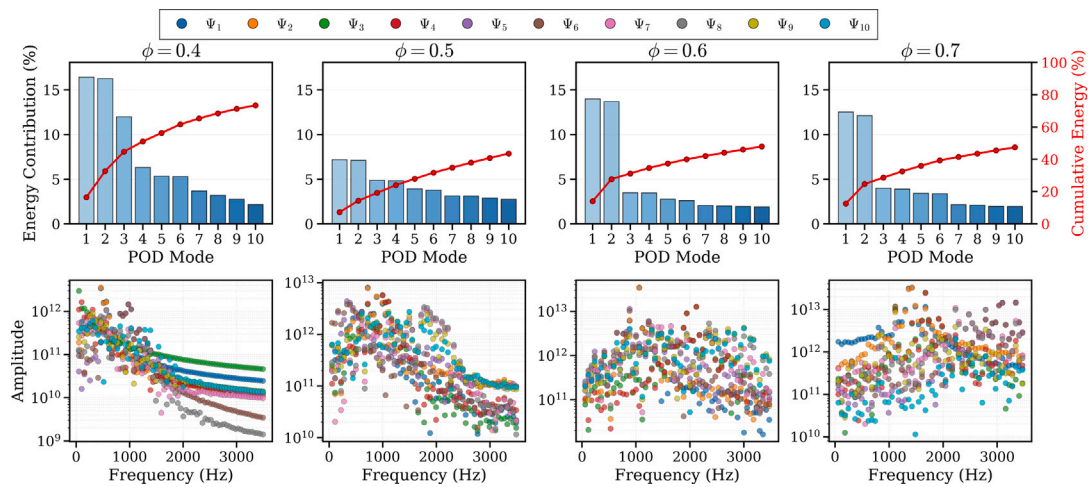


Fig. 7. POD analysis of the heat release rate perturbation field for several equivalence ratios ($\phi = 0.4\text{--}0.7$) for the cases with Soret effect. The top row shows the energy contribution of the first ten POD modes, with cumulative energy plotted in red. The bottom row presents the frequency spectra of the temporal coefficients for each mode. (For interpretation of the references to color in this figure legend, the reader is referred to the web version of this article.)

reflect flame–volume oscillations that are often acoustically driven or associated with global flame–pressure coupling. Deformation modes, similarly unpaired, describe localized distortions of the flame surface without net convective transport.

We first isolate the diffusion modeling effect at fixed equivalence ratio ($\phi = 0.6$), then examine the equivalence ratio trend with a single diffusion model. This approach shows that our mechanistic conclusions arise from the comparison of transport models, i.e., Unity Lewis vs. W/o. Soret vs. W. Soret, not from the interpretation of a single POD mode in isolation.

4.4.1. Diffusion modeling effect

Fig. 6 examines the impact of different diffusion models at a fixed fuel–air equivalence ratio $\phi = 0.6$.

In the following, we apply two criteria across the three transport models – Unity Lewis, W/o. Soret, W. Soret: (i) leading-pair invariance: near-constancy of the dominant frequency of $a_{1,2}(t)$ and strong overlap of the leading subspace with the Unity Lewis baseline, which is interpreted as hydrodynamic drive; and (ii) energy compactness: large $E_1 + E_2$ and a high cumulative share in the first modes, whose loss, i.e., broadening/redistribution into higher modes, signals modulation by non-equidiffusion and the absence of a single dominant mechanism.

All three cases show dominant contributions from the first two POD modes, but with varying degrees of energy concentration. The Unity Lewis case exhibits the most compact energy distribution with nearly 50% of the total energy captured by the first two modes, and approximately 70% within the first six modes, consistent with highly organized dynamics dominated by large-scale convective structures. Including differential-preferential diffusion, i.e., W/o. Soret, broadens the spectrum, approximately 10 modes are required to capture a comparable 60% of the energy, although energy still remains focused in the leading modes. Reintroducing thermodiffusion, i.e., W. Soret, partially restores modal compactness at this equivalence ratio, though the extent of this recovery varies with ϕ as detailed in the Supplementary Material. At lean conditions ($\phi \leq 0.5$), thermal diffusion amplifies multi-scale cellular structures, thereby spreading energy more broadly than differential-preferential diffusion alone. At $\phi = 0.6$, however, the Soret effect appears to partially counteract the dispersive influence of differential-preferential diffusion, resulting in intermediate energy concentration. This non-monotonic dependence likely reflects a transition in the balance between thermodiffusive and hydrodynamic mechanisms.

Frequency analysis of the temporal coefficients confirms this pattern. The Unity Lewis case displays narrowband peaks in the first two

modes and limited broadband content at other frequencies. In contrast, the W/o. Soret and W. Soret cases show increasingly broad spectral distributions, especially in higher-order modes. Furthermore, while the Unity Lewis case shows a dominant frequency near 1200 Hz in modes Ψ_1 and Ψ_2 , the other two cases exhibit a downward spectral shift with peaks closer to 1050 Hz. As noted in Section 4.3, the magnitude of these shifts cannot be explained by bulk advection alone (see Table 1), indicating that diffusion physics drives the frequency change. These leading modes, given their energetic dominance and spectral alignment with the observed acoustic peaks, likely contribute significantly to the sound generation, a connection explored in detail in Section 4.4.3. This suggests that thermal and differential-preferential diffusion enhance modulation and facilitate coupling between coexisting instability mechanisms, reshaping the spectral distribution without altering the spatial organization of the leading convective pair.

Additionally, the Unity Lewis case exhibits clear higher-order harmonics in modes Ψ_3 and Ψ_4 at approximately twice the base frequency. This structured spectral content reflects coherent, periodic flame dynamics governed by nonlinear self-excited oscillations. These harmonics are absent or suppressed in the other cases, consistent with added transport-induced phase dispersion when non-equidiffusion is enabled. The spatial structures of the POD modes for the W/o. Soret and Unity Lewis cases at $\phi = 0.6$ are shown in Fig. 8(b); the W. Soret case at $\phi = 0.6$ is included in Fig. 8(a) as part of the equivalence ratio series.

4.4.2. Equivalence–ratio trend

Having isolated modeling effects at $\phi = 0.6$, we now examine how modal energetics vary with equivalence ratio. Fig. 7 presents the energy distribution among the first ten POD modes for cases with Soret effect across all ϕ values. To interpret these trends, we apply the same criteria used in the diffusion model comparison: leading-pair invariance and energy compactness. Additional details regarding diffusion model effects are provided in the Supplementary Material.

The equivalence ratio strongly influences both energy concentration and spectral organization. At the leanest condition ($\phi = 0.4$), energy spreads broadly across modes and remains sensitive to the diffusion model, behavior consistent with strong thermodiffusive influence relative to the Unity Lewis baseline. At the intermediate case ($\phi = 0.5$), the most distributed energy spectrum emerges, reflecting competing instability mechanisms where no single process dominates. At this equivalence ratio, the Lewis number has increased sufficiently to weaken pure thermodiffusive instability relative to $\phi = 0.4$, while hydrodynamic effects remain less dominant than at richer conditions. The coexistence of these mechanisms produces a broad range of active

spatial and temporal scales. As ϕ increases to 0.6 and 0.7, the spectra become progressively more compact, with larger energy shares in the first mode pair and near-invariance across diffusion models. This compactness indicates that hydrodynamic effects increasingly govern the dynamics. Nevertheless, even for these richer flames, the first ten modes capture less than 40% of the total energy, revealing significant activity in higher-order components. This persistent energy spreading suggests that while a dominant instability emerges, it coexists with secondary spatial and temporal features, resulting in complex, multi-modal flame behavior.

The frequency spectra of the temporal coefficients corroborate these energy-based observations. At $\phi = 0.5$, a broad band of active frequencies appears across multiple modes, consistent with the energetic competition between instability processes. In contrast, both the leanest ($\phi = 0.4$) and richest ($\phi = 0.7$) flames exhibit more organized spectral signatures with sharper peaks in the leading modes. Across all equivalence ratios, several POD modes appear in pairs characterized by similar energy content and aligned dominant frequencies. These paired modes correspond to traveling wave structures. Convecting disturbances naturally decompose into nearly energy-degenerate pairs with co-spectral peaks and approximately quadrature-phase temporal coefficients which enables reconstruction of propagating flame patterns.

To connect the spectral trends with spatial organization, we summarize next the spatial POD structures at $\phi = 0.4$ (W. Soret) shown in Fig. 8(a). The spatial structures can be described in four mode families: convective (C) modes correspond to downstream translation of coherent structures, typically associated with wrinkle advection. Breathing (B) modes represent quasi-symmetric expansion and contraction of the flame front about its mean position, reflecting global oscillations in flame area and intensity and necessarily producing a net change in total flame area. Deformation (D) modes capture push-pull redistributions of the front with alternating regions of outward and inward displacement along the span; they may remain globally symmetric and may or may not change total area depending on the weighting of these regions. Finally, Modulated/Complex (M) modes exhibit superposed or mixed spatial-temporal behavior (e.g., concurrent convection and breathing, or higher-harmonic modulation).

The spatial structures of the POD modes for $\phi = 0.4$ shown in Fig. 8(a) reveal distinct physical mechanisms underlying the flame dynamics. The leading modes exhibit well-organized patterns aligned with the flame front and can be grouped by their spatial and temporal characteristics. The first two modes Ψ_1 and Ψ_2 form a canonical convective pair. Their spatial patterns show downstream-shifting wave-like features and their temporal coefficients peak at a shared dominant frequency. These observations are consistent with convective behavior, i.e., paired, near-degenerate energies; co-spectral peaks; and phase-shifted temporal coefficients. A second convective pair appears in modes Ψ_5 and Ψ_6 that are characterized by higher spatial frequency and shorter wavelength structures, which is consistent with smaller-scale traveling waves. The spatial organization of these modes is qualitatively consistent with the fine cellular structures observed in the corresponding flames (Fig. 2), suggesting that the POD decomposition captures the multi-scale flame organization arising from diffusion-driven instabilities.

In contrast, mode Ψ_3 exhibits a symmetric structure across the flame and lacks downstream phase progression, suggesting little spatial convection in its underlying physical mechanism, i.e., global, in-phase fluctuations without directional phase advance. Its frequency content is concentrated around a single peak as shown in Fig. 8, consistent with a global breathing or pulsating mode. Mode Ψ_4 also lacks a spatially shifted partner. Instead, it appears localized and oscillatory along the flame front which suggests a deformation or surface fluctuation mode not associated with convection. Therefore, only movement normal to the flame surface is captured. Finally, higher-order modes like Ψ_7 and Ψ_8 are more spatially intricate and energetically weaker, but feature layered patterns transverse to the flame and broadband spectral content. These indicate modulated or nonlinear behavior that possibly reflects interactions between multiple instability mechanisms.

Table 2

Classification of the first eight POD modes of the heat release rate field based on their dominant physical behavior for several equivalence ratios ϕ . Mode types: Convective (C), Breathing (B), Deformation (D), and Modulated/Complex (M).

Mode #	$\phi = 0.4$	$\phi = 0.5$	$\phi = 0.6$	$\phi = 0.7$
1	(C)	(C)	(C)	(C)
2	(C)	(C)	(C)	(C)
3	(B)	(C)	(C)	(M)
4	(D)	(C)	(C)	(M)
5	(C)	(M)	(M)	(C)
6	(C)	(M)	(M)	(C)
7	(M)	(M)	(M)	(M)
8	(M)	(M)	(M)	(M)

To consolidate these interpretations across all studied conditions, Table 2 classifies the first eight POD modes at each ϕ based on their dominant behavior. With increasing equivalence ratio, convective modes progressively dominate the energetic budget, while purely breathing or deformation modes vanish from the leading contributions. In this context, the breathing motion corresponds to a low-frequency modulation with strong variation of the heat release rate driven by flame-area changes; at higher ϕ its contribution is increasingly dwarfed by convective dynamics, a trend corroborated by the SPL, where low-frequency content weakens while the convective peak at higher frequencies strengthens.

4.4.3. Modal analysis and sound pressure coupling

A comparison between the POD results and the SPL spectra in Fig. 5 offers further insight into the acoustic relevance of the dominant heat release dynamics. At lower equivalence ratios, such as $\phi = 0.4$, the SPL amplitude is modest and primarily associated with low-frequency content. This result correlates well with the POD analysis, where the leading modes exhibit convective and breathing dynamics with peak frequencies in the sub-kilohertz range. As ϕ increases, both the SPL amplitude and spectral complexity grow, leading to more energetic and broadband excitation of the acoustic field. The POD results mirror this trend through increased modal energy spreading and the emergence of multi-scale wrinkling features.

At $\phi = 0.6$, a clear alignment is observed between the dominant POD frequencies (Fig. 6) and the acoustic response for all diffusion models. In each case, a prominent spectral peak between 1050 and 1200 Hz appears in both the POD and SPL spectra, indicating a hydrodynamic instability that consistently governs the acoustic emission. This peak is sharpest in the Unity Lewis model and reflects the strong energy localization in the leading POD modes. With differential-preferential diffusion (W/o. Soret), the peak remains present but is slightly diminished, while the inclusion of thermodiffusion (W. Soret) broadens the response and shifts a portion of the energy toward higher-order modes. Although the spectral shape varies across diffusion models, the core instability remains the primary acoustic source in all cases.

To further examine the acoustic relevance of the spatial structures revealed by the POD, a coherence survey between pressure and heat release dynamics was performed for the $\phi = 0.6$, W. Soret case (Supplementary Material, Fig. 12). The results confirm that acoustic emission is governed predominantly by the lowest-order heat release modes, which represent global flame shape changes and large-scale wrinkling motion. The strongest coherence occurs in a narrow band near 1–1.2 kHz, consistent with the dominant radiated SPL. In contrast, higher-index modes, associated with localized curvature variations and small-scale perturbations in the burning rate, exhibit negligible acoustic coherence, indicating that such fine-scale features contribute minimally to the emitted sound. The same methodology may be applied to the remaining conditions; however, only this representative case is reported here for brevity.

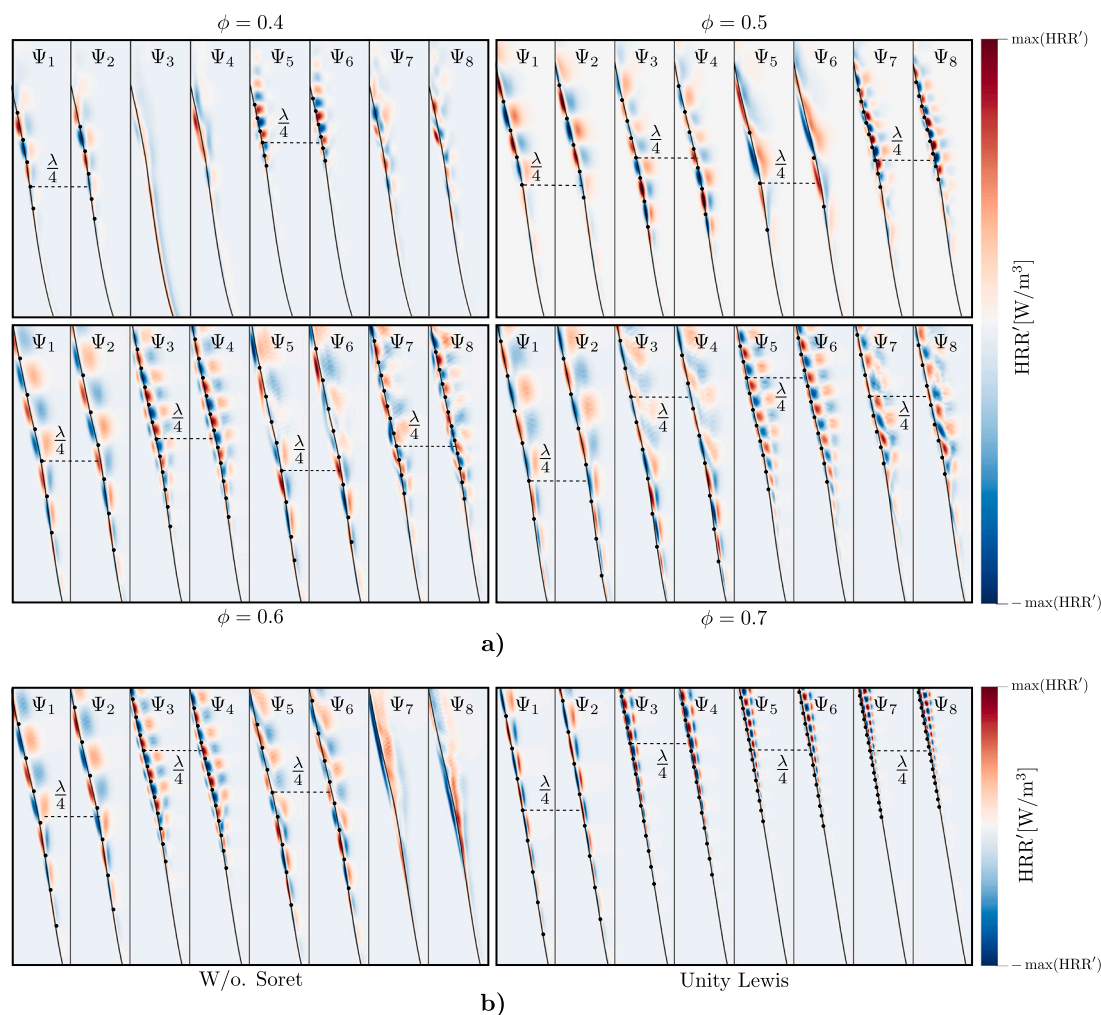


Fig. 8. First eight spatial POD modes Ψ_1 – Ψ_8 of (a) the heat release rate fluctuations for varying equivalence ratios $\phi = 0.4$ – 0.7 using the W. Soret model and (b) W/o. Soret and Unity Lewis case results for the $\phi = 0.6$ case (W. Soret can be referred to in (a)). Each mode is normalized by its maximum and shown with a consistent colormap for direct comparison. Black dots represent the nodal points of the spatial distribution. Dashed lines indicate a characteristic phase shift of $\lambda/4$ where applicable, highlighting convective structures. The black line shows the time-averaged flame front extracted at progress variable $C = 0.5$. (For interpretation of the references to color in this figure legend, the reader is referred to the web version of this article.)

These results demonstrate that while thermodiffusive and differential-preferential diffusion effects do not suppress the underlying flame instabilities, they significantly reshape their spectral organization by altering phase relationships and energy distribution among dominant modes. Consequently, the acoustic emission frequency can shift away from the natural mode frequency toward one shaped by diffusion-driven interactions. Although the underlying instability – whether hydrodynamic or thermodiffusive – remains active, non-equidiffusion modifies how it develops, how energy is partitioned across modes, and how effectively it couples to the acoustic field.

However, while POD effectively captures the dominant spatial structures of flame dynamics, it ranks modes purely by their energetic contribution and does not explicitly resolve temporal coherence or frequency content. Acoustically relevant features that manifest at lower energy levels or arise from modal interactions may therefore be masked, particularly in cases with detailed diffusion modeling where energetic modes interact but are not easily separable through POD alone. To address this limitation, we complement the POD analysis with DMD, which directly identifies coherent oscillatory structures with fixed temporal frequencies and growth rates, providing insight into how diffusion effects determine the temporal organization and spectral content of the flame dynamics in relation to the observed acoustic response.

4.5. Dynamic mode decomposition analysis

To further investigate the temporal organization of flame dynamics and to validate the trends observed in the POD analysis, Dynamic Mode Decomposition (DMD) is applied to the HRR field across all equivalence ratios and diffusion models. DMD extracts modes characterized by fixed frequencies and growth rates, such that dominant spectral structures and their evolution under varying transport conditions can be identified.

As shown in Fig. 9, Dynamic Mode Decomposition of the HRR field yields continuous-time eigenvalues $\lambda_j = \sigma_j + i\omega_j$ with growth rates close to zero ($|\sigma_j| \lesssim \mathcal{O}(10^{-8}) \text{ s}^{-1}$), so $|\sigma_j|T_{\text{obs}} \ll 1$ and the dominant oscillations are effectively neutral over the record. For the investigated slit flame configuration, this near-zero growth behavior reflects two key physical mechanisms. First, instabilities have finite residence time. Perturbations grow as they convect along the flame but are continuously advected downstream and leave the domain at the flame tip, preventing unbounded amplification. Second, nonlinear effects including flame curvature, stretch, and local heat losses limit spatial growth before advection removes the structures. The near-zero growth rates thus indicate a statistically stationary state where instability generation, spatial growth, saturation, and advective removal balance. The near-zero growth behavior was verified to be robust with respect to the

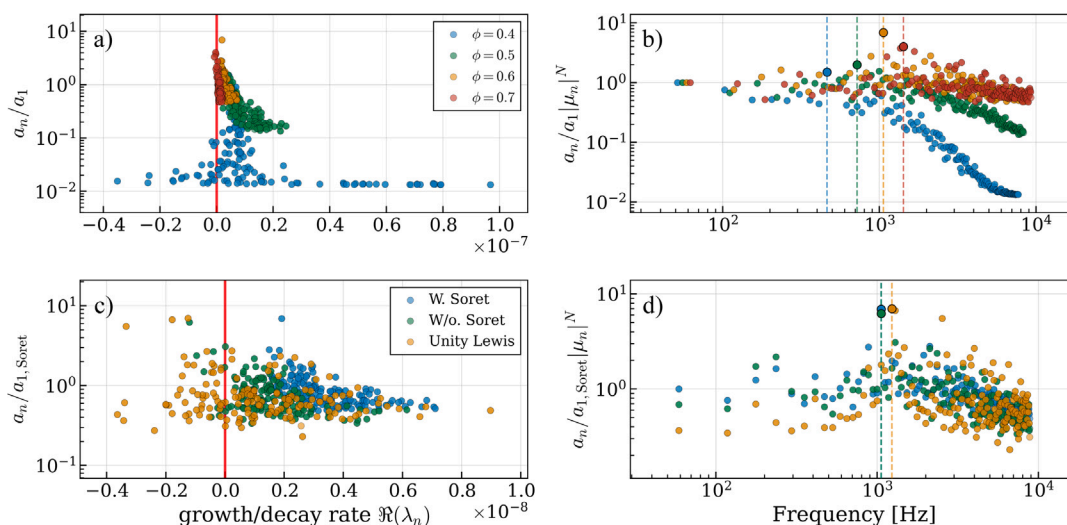


Fig. 9. Dynamic Mode Decomposition of the HRR fluctuations for varying equivalence ratios ($\phi = 0.4$ – 0.7) and diffusion models at $\phi = 0.6$. (a,b) Mode amplitude normalized by the leading mode amplitude of the same case (a_n/a_1) as a function of (a) the real part of the eigenvalues $\Re(\lambda_n)$, indicating growth or decay rates, and (b) frequency, showing the spectral content of the dominant modes. (c,d) Mode amplitude normalized by the leading mode amplitude of the W. Soret case ($a_n/a_{1,\text{Soret}}$) for each diffusion model, plotted as a function of (c) growth/decay rate and (d) frequency. The vertical red line in (a,c) marks the zero growth rate threshold. Dashed vertical lines in (b,d) indicate the dominant frequency for each ϕ value. (For interpretation of the references to color in this figure legend, the reader is referred to the web version of this article.)

chosen time-series length and window configuration, confirming that the observed marginal stability reflects a physical property of the flow rather than a numerical artifact of the DMD procedure. This has two important implications: (i) the observed dynamics represent persistent spatial patterns maintained by continuous generation and advection, capturing the intrinsic flame response under each transport model, and (ii) the consistency of this state across all equivalence ratios and diffusion models allows meaningful comparison of mode amplitudes and spectral content. This behavior is consistent with the statistically stationary temporal coefficients observed in the POD analysis.

The spectral content of the DMD modes reflects a clear trend with increasing equivalence ratio. Leaner flames exhibit narrowband, low-frequency dynamics, while richer flames show progressively broader frequency spectra with multiple energetic peaks. This progression mirrors the increased spatial complexity and energy spreading across POD modes and substantiates the picture of richer flames being governed by multiple interacting instability mechanisms.

At the fixed equivalence ratio $\phi = 0.6$, DMD highlights how the diffusion model shapes the spectral alignment and energy content of dominant flame modes. The Unity Lewis case exhibits a sharp primary peak near 1200 Hz which is accompanied by a distinct secondary peak near 2400 Hz. This indicates the presence of a second harmonic. This structured spectral signature reflects highly coherent, periodic dynamics governed by nonlinear self-excited oscillations. Non-equidiffusive effects shift the dominant peak downward and disperse the energy across a wider frequency range. DMD results for $\phi = 0.4$, 0.5 , and 0.7 can be found in the Supplementary Material. Overall, the DMD shows that the dominant instability, typically hydrodynamic in richer flames, persists across all diffusion models, while its spectral signature is shaped by transport: differential-preferential and thermal diffusion redistribute energy across frequencies and thereby modify mode selection and coherence.

Conclusions

This study presents a detailed numerical investigation of the influence of non-equidiffusion on the flame dynamics and acoustic response of premixed hydrogen–air slit flames. Using two-dimensional direct numerical simulations across a range of equivalence ratios ($\phi =$

$0.4, 0.5, 0.6, 0.7$) and diffusion models, the effects of thermal and differential-preferential diffusion are systematically evaluated.

The results show that differential-preferential and thermal diffusion mechanisms significantly affect hydrogen–air slit flame structure, particularly under lean conditions. The inclusion of the Soret effect leads to sharper flame cusps and cellular structures, while the Unity Lewis number approximation suppresses these features and fails to capture localized superadiabatic temperatures. The flame’s overall structure, dynamics, and cell size distribution are shown to be sensitive to the diffusion model. Richer mixtures exhibit broader cellular scales dominated by hydrodynamic instabilities.

POD and DMD spectral analyses of the acoustic field reveal that diffusion modeling strongly influences the flame’s acoustic response, primarily by altering the organization and interaction of coherent structures. Across all equivalence ratios, the inclusion of preferential and thermal diffusion modifies the spectral characteristics of the dominant modes and redistributes energy across interacting structures. At richer conditions, hydrodynamic instabilities remain dominant, but the inclusion of additional diffusion effects still modifies the energetic distribution and temporal coherence of the response. These effects are particularly evident at intermediate equivalence ratios, where diffusion alters how energy is partitioned among modes, leading to spectral shifts and changes in acoustic intensity. In particular, the effects of thermal diffusion on the organization of energetic modes are found to be dependent on the equivalence ratio, with different behavior at the leaner and richer ends of the studied equivalence ratio range. Furthermore, these findings emphasize that the acoustic manifestation of flame dynamics is governed by the type of instability and by how transport properties modulate the flame structure, coherence, and spectral expression. Even when hydrodynamic instabilities dominate, their physical behavior remains sensitive to the diffusion model, which influences how energy is distributed among modes and how strongly they couple to the acoustic field. Therefore, it is essential to accurately capture preferential and thermal diffusion to resolve the correct dynamic response and sound generation in premixed hydrogen flames. Simplified models may miss key modal interactions and underpredict the resulting acoustic emissions.

While the present slit-flame configuration is intentionally canonical, it is designed to isolate and quantify the fundamental mechanisms of diffusion acoustic coupling without geometric or turbulent complexity.

The resulting insights provide a physically interpretable foundation for understanding how preferential and thermal diffusion influence flame acoustic interactions. Building on this framework, future work would be to extend the analysis toward three-dimensional and more realistic combustor geometries, where these mechanisms interact with turbulence and confinement effects to shape the overall thermoacoustic response.

CRedit authorship contribution statement

Borja Pedro-Beltran: Writing – original draft, Visualization, Software, Methodology, Formal analysis, Data curation, Conceptualization. **Zin Shahin:** Writing – original draft, Visualization, Software, Methodology, Formal analysis, Data curation, Conceptualization. **Matthias Meinke:** Writing – review & editing, Supervision, Resources. **Sohel Herff:** Writing – review & editing, Supervision. **Dominik Krug:** Writing – review & editing, Supervision. **Wolfgang Schröder:** Writing – review & editing, Supervision, Resources, Project administration, Funding acquisition.

Declaration of competing interest

The authors declare that they have no known competing financial interests or personal relationships that could have appeared to influence the work reported in this paper.

Acknowledgments

The authors gratefully acknowledge the funding of the Deutsche Forschungsgemeinschaft (DFG, German Research Foundation) under grant number SCHR 309/81-1 and grant number IRTG 2983 (Hy-Potential: Hydrogen - Fundamentals of Production, Storage & Transport, Applications, and Economy). Computational resources were provided by CSC – IT Center for Science (Finland) and the Gauss Centre for Supercomputing e.V. (www.gauss-centre.eu), enabling access to the Mahti supercomputer and the GCS system HAWK/HUNTER at the High-Performance Computing Center Stuttgart (HLRS) (www.hlrs.de), which made the large-scale simulations in this study possible.

Appendix A. Supplementary data

Supplementary material related to this article can be found online at <https://doi.org/10.1016/j.combustflame.2026.114810>.

References

- [1] H. Pitsch, The transition to sustainable combustion: Hydrogen- and carbon-based future fuels and methods for dealing with their challenges, *Proc. Combust. Inst.* 40 (2024) 105638.
- [2] T. Boushaki, Y. Dhué, L. Selle, B. Ferret, T. Poinso, Effects of hydrogen and steam addition on laminar burning velocity of methane-air premixed flame: experimental and numerical analysis, *Int. J. Hydrog. Energy* 37 (2012) 9412–9422.
- [3] A.M. Garcia, S. Le Bras, J. Prager, I. Boxx, W. Polifke, Impact of H₂-enrichment on the response of a partially premixed CH₄-air flame to velocity and equivalence ratio fluctuations, *Combust. Flame* 268 (2024) 113595.
- [4] T. Lieuwen, *Unsteady Combustor Physics*, Cambridge University Press, 2012.
- [5] E. Karlis, Y. Liu, Y. Hardalupas, A.M. Taylor, H₂ enrichment of CH₄ blends in lean premixed gas turbine combustion: An experimental study on effects on flame shape and thermoacoustic oscillation dynamics, *Fuel* 254 (2019) 115524.
- [6] J. Beita, M. Talibi, S. Sadasivuni, R. Balachandran, Thermoacoustic instability considerations for high hydrogen combustion in lean premixed gas turbine combustors: A review, *Hydrogen* 2 (1) (2021) 33–57.
- [7] J. Zhang, A. Ratner, Experimental study of the effects of hydrogen addition on thermoacoustic instability in a variable-length combustor, *Int. J. Hydrog. Energy* 46 (2021) 16086–16098.
- [8] M. Matalon, Intrinsic flame instabilities in premixed and nonpremixed combustion, *Annu. Rev. Fluid Mech.* 39 (2007) 163–191.
- [9] A. Michalke, Survey on jet instability theory, *Prog. Aerosp. Sci.* 21 (3) (1984) 159–199.
- [10] A.J. Aspden, M.S. Day, J.B. Bell, Turbulence–flame interactions in lean premixed hydrogen: Transition to the distributed burning regime, *J. Fluid Mech.* 680 (2011) 287–320.
- [11] F.A. Williams, *Combustion Theory*, CRC Press, 2018.
- [12] A. Aspden, M. Day, J. Bell, Characterization of low lewis number flames, *Proc. Combust. Inst.* 33 (2011) 1463–1471.
- [13] A. Lipatnikov, *Fundamentals of Premixed Turbulent Combustion*, Taylor & Francis, 2012.
- [14] S.M. Correa, A review of NO_x formation under gas-turbine combustion conditions, *Combust. Sci. Technol.* 87 (1993) 329–362.
- [15] A. Dupuy, Q. Douasbin, T. Poinso, Control of intrinsic ThermoAcoustic instabilities for methane and hydrogen air flames: DNS and network analysis, *Proc. Combust. Inst.* 40 (2024) 105217.
- [16] M. Talei, E.R. Hawkes, M.J. Brear, A direct numerical simulation study of frequency and lewis number effects on sound generation by two-dimensional forced laminar premixed flames, *Proc. Combust. Inst.* 34 (2013) 1093–1100.
- [17] S. Schlimpert, S. Hemchandra, M. Meinke, W. Schröder, Hydrodynamic instability and shear layer effect on the response of an acoustically excited laminar premixed flame, *Combust. Flame* 162 (2015) 345–367.
- [18] S. Schlimpert, M. Meinke, W. Schröder, Nonlinear analysis of an acoustically excited laminar premixed flame, *Combust. Flame* 163 (2016) 337–357.
- [19] J. Masugi, T. Shoji, Y. Nakazumi, R. Fujii, T. Tomidokoro, S. Tachibana, T. Yokomori, Lewis number effect in lean premixed H₂-air and CH₄-air flames during thermoacoustic instability in a low-swirl combustor, *Phys. Rev. Fluids* 10 (2025) 043201.
- [20] F.H. Vance, c. Alanyalıoğlu, C. Hasse, Analysis of lewis number effects on dynamic response of laminar premixed flames, *Combust. Flame* 248 (2023) 112508.
- [21] B. Pedro Beltran, M. Meinke, W. Schröder, Acoustic emission of thermodynamic unstable premixed lean hydrogen-air slit flames, in: 30th AIAA/CEAS Aeroacoustics Conference, 2024, p. 3191.
- [22] F. Fruzza, H. Chu, R. Lamioni, T. Grenga, C. Galletti, H. Pitsch, The importance of Soret effect, preferential diffusion, and conjugate heat transfer for flashback limits of hydrogen-fueled perforated burners, *Proc. Combust. Inst.* 40 (2024) 105581.
- [23] T. Poinso, D. Veynante, *Theoretical and Numerical Combustion*, Edwards, 2005.
- [24] B. van Leer, Towards the ultimate conservative difference scheme. V.A second-order sequel to Godunov's method, *J. Comput. Phys.* 32 (1979) 101–136.
- [25] M.-S. Liou, C.J. Steffen, A new flux splitting scheme, *J. Comput. Phys.* 107 (1993) 23–39.
- [26] L. Schneiders, C. Günther, M. Meinke, W. Schröder, An efficient conservative cut-cell method for rigid bodies interacting with viscous compressible flows, *J. Comput. Phys.* 311 (2016) 62–86.
- [27] B. McBride, S. Gordon, M. Reno, Coefficients for Calculating Thermodynamic and Transport Properties of Individual Species, NASA, Report No. TM-4513, 1993.
- [28] R.J. Kee, M.E. Coltrin, P. Glarborg, H. Zu, *Chemically Reacting Flows: Theory, Modeling, and Simulation*, second ed., John Wiley and Sons, 2018.
- [29] J. Schlup, G. Blanquart, A reduced thermal diffusion model for H and H₂, *Combust. Flame* 191 (2018) 1–8.
- [30] K. Pausch, S. Herff, W. Schröder, Noise sources of an unconfined and a confined swirl burner, *J. Sound. Vib.* 475 (2020) 115293.
- [31] B.P. Beltran, S. Herff, K. Pausch, M. Meinke, W. Schröder, Analysis of the impact of chemistry models on the non-equidiffusion effects of lean premixed hydrogen flames, in: AIAA Scitech Forum, 2022.
- [32] J. Li, Z. Zhao, A. Kazakov, F.L. Dryer, An updated comprehensive kinetic model of hydrogen combustion, *Int. J. Chem. Kinet.* 36 (2004) 566–575.
- [33] F.H. Vance, A. Scholtissek, P. de Goey, J. van Oijen, C. Hasse, Dynamic stabilization of a hydrogen premixed flame in a narrow channel, *Combust. Flame* 248 (2023) 112560.
- [34] K.E. Niemeyer, N.J. Curtis, C.-J. Sung, pyJac: Analytical Jacobian generator for chemical kinetics, *Comput. Phys. Comm.* 215 (2017) 188–203.
- [35] Institute of Aerodynamics, m-AIA (v2024.1), 2024, <http://dx.doi.org/10.5281/zenodo.13350586>.
- [36] A.C. Hindmarsh, P.N. Brown, K.E. Grant, S.L. Lee, R. Serban, D.E. Shumaker, C.S. Woodward, SUNDIALS: Suite of nonlinear and differential/algebraic equation solvers, *ACM Trans. Math. Softw.* 31 (2005) 363–396.
- [37] K. Taira, S.L. Brunton, S.T. Dawson, C.W. Rowley, T. Colonius, B.J. McKeon, O.T. Schmidt, S. Gordeyev, V. Theofilis, L.S. Ukeiley, Modal analysis of fluid flows: An overview, *AIAA J.* 55 (2017) 4013–4041.
- [38] P.J. Schmid, Dynamic mode decomposition of numerical and experimental data, *J. Fluid Mech.* 656 (2010) 5–28.
- [39] D. Hwang, K. Ahn, Y. Yoon, Flame length scaling of C₂H₄-air premixed flames under acoustic forcing, *J. Appl. Fluid Mech.* 11 (2018) 647–654.
- [40] S. Shi, A. Breicher, R. Schultheis, S. Hartl, R.S. Barlow, D. Geyer, A. Dreizler, Structures of laminar lean premixed H₂/CH₄/air polyhedral flames: Effects of flow velocity, H₂ content and equivalence ratio, *Flow Turbul. Combust.* 113 (4) (2024) 1081–1110.
- [41] S. Herff, K. Pausch, H. Nawroth, S. Schlimpert, C. Paschereit, W. Schröder, Impact of burner plenum acoustics on the sound emission of a turbulent lean premixed open flame, *Int. J. Spray Combust.* 12 (2020) 1756827720956906.

- [42] F. Frizza, R. Lamioni, L. Tognotti, C. Galletti, Flashback of H₂-enriched premixed flames in perforated burners: Numerical prediction of critical velocity, *Int. J. Hydrog. Energy* 48 (81) (2023) 31790–31801.
- [43] F.H. Vance, L. De Goey, J.A. van Oijen, Development of a flashback correlation for burner-stabilized hydrogen-air premixed flames, *Combust. Flame* 243 (2022) 112045.
- [44] G. Lodato, P. Domingo, L. Vervisch, Three-dimensional boundary conditions for direct and large-eddy simulation of compressible viscous flows, *J. Comput. Phys.* 227 (2008) 5105–5143.
- [45] T. Zirwes, F. Zhang, T.L. Kaiser, K. Oberleithner, O.T. Stein, H. Bockhorn, A. Kronenburg, The role of thermodiffusion and dimensionality in the formation of cellular instabilities in hydrogen flames, *Proc. Combust. Inst.* 40 (2024) 105665.
- [46] L. Berger, K. Kleinheinz, A. Attili, H. Pitsch, Characteristic patterns of thermodiffusively unstable premixed lean hydrogen flames, *Proc. Combust. Inst.* 37 (2019) 1879–1886.
- [47] A. Albayrak, R.S. Blumenthal, A. Ulhaq, W. Polifke, An analytical model for the impulse response of laminar premixed flames to equivalence ratio perturbations, *Proc. Combust. Inst.* 36 (3) (2017) 3725–3732.
- [48] M. Talei, E.R. Hawkes, M.J. Brear, A direct numerical simulation study of frequency and Lewis number effects on sound generation by two-dimensional forced laminar premixed flames, *Proc. Combust. Inst.* 34 (1) (2013) 1093–1100.
- [49] A. Haghiri, M. Talei, M.J. Brear, E.R. Hawkes, Sound generation by turbulent premixed flames, *J. Fluid Mech.* 843 (2018) 29–52.
- [50] S. Candel, D. Durox, S. Ducruix, A.-L. Birbaud, N. Noiray, T. Schuller, Flame dynamics and combustion noise: Progress and challenges, *Int. J. Aeroacoust.* 8 (2009) 1–56.
- [51] M. Rodríguez-Pastor, P. Koumides, E.J. Pérez-Sánchez, J. García-Tíscar, A. Broatch, D. Mira, Numerical analysis of laminar velocity-forced premixed slit flames using modal decomposition techniques, *Combust. Flame* 269 (2024) 113661.